Journal of the European Ceramic Society 41 (2021) 6883–6893

Contents lists available at ScienceDirect

Journal of the European Ceramic Society

journal homepage: www.elsevier.com/locate/jeurceramsoc

Original Article

Interpreting acoustic energy emission in SiC/SiC minicomposites through modeling of fracture surface areas

B. Swaminathan [a], N.R. McCarthy [b], A.S. Almansour [c], K. Sevener [d], A.K. Musaffar [b], T.M. Pollock [a], J.D. Kiser [c], S. Daly [b,*]

[a] Materials Department, University of California, Santa Barbara, Engineering II, Santa Barbara, CA, 93106, USA
[b] Department of Mechanical Engineering, University of California, Santa Barbara, Engineering II, Santa Barbara, CA, 93106, USA
[c] NASA Glenn Research Center (GRC), 21000 Brookpark Road, Cleveland, OH, 44135, USA
[d] Department of Materials Science and Engineering, University of Michigan, 2300 Hayward St, Ann Arbor, MI, 48109, USA

ARTICLE INFO

Keywords:
Acoustic emission
Ceramic matrix composite
Crack propagation
Silicon carbide
Micromechanical modeling

ABSTRACT

The relationship between acoustic emission (AE) and damage source areas in SiC/SiC minicomposites was modeled using insights from tensile testing in-scanning electron microscope (SEM). Damage *up to* matrix crack saturation was bounded by: (1) AE generated by matrix cracking (lower bound) and (2) AE generated by matrix cracking, and fiber debonding and sliding in crack wakes (upper bound). While fiber debonding and sliding exhibit lower strain energy release rates than matrix cracking and fiber breakage, they contribute significant damage area and likely produce AE. Fiber breaks *beyond* matrix crack saturation were modeled by two conditions: (i) *only* fiber breaks generated AE; and (ii) fiber breaks occurred simultaneously with fiber sliding to generate AE. While fiber breaks are considered the dominant late-stage mechanism, our modeling indicates that other mechanisms are active, a finding that is supported by experimental in-SEM observations of matrix cracking in conjunction with fiber failure at rupture.

1. Introduction

Silicon carbide / silicon carbide ceramic matrix composites (SiC/SiC CMCs) are characterized by high stiffness, low weight, and damage tolerance [1]. In CMCs, damage can be considered to occur over two domains. First, damage initiates and accumulates in the matrix, where crack initiation and propagation create new surfaces. Crack deflection at interphases leads to fiber debonding and sliding, which are considered secondary damage mechanisms, to locally relieve stress. In the second domain, after matrix crack saturation, load is structurally carried by fibers, which break and create new surfaces up to failure. Fiber tow rupture at failure, in combination with local matrix cracking and additional fiber breaks near the rupture area, all create new surfaces [2–4].

A non-destructive approach to characterize damage is acoustic emission (AE), which captures the elastic waves generated by the local strain energy released from damage events [5]. AE is well-suited for capturing brittle and distinct damage mechanisms, such as matrix cracking and fiber breaks. One theory is that the 'loudness' of an AE event (i.e. its energy or amplitude) corresponds to the surface area created by its damage source [5]. As such, the total AE energy generated by a mechanism is related to the total area created by its occurrences; this is supported by a relationship between AE energy accumulation and measured crack surface area in SiC/SiC [6]. Although the energy of an AE event is influenced by transducer contact to the specimen, relative AE energies are unaffected for a given test, enabling a comparison of AE events generated in a single specimen.

This work relates damage progression to AE energy accumulation in order to estimate the surface area created by each AE event in SiC/SiC minicomposites, using insights gained from combining AE measurements with in-SEM (scanning electron microscope) mechanical testing [7] and certain assumptions on specimen geometry and damage mechanisms. Two scenarios are considered, where (i) AE is only sensitive to the occurrence of dominant damage mechanisms (and event energies represent the surfaces created by dominant mechanisms), or (ii) AE is sensitive to the occurrence of both dominant and secondary (non-dominant) mechanisms (and event energies represent the surfaces created by dominant and non-dominant mechanisms). To investigate these possibilities, we develop a set of boundary conditions which bisect

* Corresponding author.
E-mail address: samdaly@ucsb.edu (S. Daly).

https://doi.org/10.1016/j.jeurceramsoc.2021.06.030
Received 26 January 2021; Received in revised form 2 June 2021; Accepted 23 June 2021
Available online 25 June 2021

the lifetime of the material in the stress domain. The cumulative damage area *up to* matrix crack saturation (Domain I) was related to the AE energy considering two scenarios: a **lower bound**, where AE is only sensitive to matrix cracking; and an **upper bound**, where AE is sensitive to the simultaneous occurrence of matrix cracking, interfacial debonding, and sliding. A second set of scenarios was used to estimate the fiber break distribution using assumptions of damage progression *after* matrix crack saturation (Domain II): **a first condition**, where AE is only sensitive to fiber failure (corresponding to the lower bound); and (ii) a **second condition**, where AE is sensitive to the simultaneous occurrence of fiber failure and sliding (corresponding to the upper bound).

2. Methods and materials

Specimens of two CVI (chemical vapor infiltrated) SiC/SiC minicomposite systems described in [7] were incrementally loaded to failure in-SEM (MIRA3, Tescan, Kohoutovice, Czech Republic) using a small tensile load frame (Kammrath & Weiss, Dortmund, Germany) with a 500 N load cell. During testing, images of the specimen surface were captured during load holds to form gage-length micrographs of surface damage accumulation. Both systems consisted of a Hi-Nicalon Type S™ (HNS) (NGS Advanced Fibers Co., Ltd., Toyama, Japan) 500 filament SiC fiber tow, a boron nitride (BN) interphase, and a SiC matrix. The interphase thicknesses and matrix volume fractions varied between systems. One system is referred to as high fiber content (HFC) due to its lower matrix content and higher fiber volume fraction, while the other is referred to as low fiber volume content (LFC) due to its lower fiber volume fraction. Each specimen's average cross-sectional area (A_c) was determined by [8]. Average interfacial parameters Γ (debond toughness) and τ (interfacial shear stress) were determined from fiber-push in testing in [7]. Properties are provided in Table 1.

AE activity was monitored using a four-channel fracture wave detection system (Digital Wave Corporation, Centennial, CO, USA). AE waveforms were recorded using two S9225 piezoelectric AE transducers (Physical Acoustics, Princeton, NJ, USA) with 300−1800 kHz sensitivity that were coupled to the specimen surface using vacuum grease. The signal energy of an event was calculated as the average of the energies at both AE sensors to (i) account for energy attenuation due to waveform propagation, and (ii) allow comparison of damage mechanisms of the same estimated size. In regard to (i), Morscher et al. found that waveforms in a CMC could lose over half their signal energy when propagating to the sensor farthest from the source; this loss increased with damage accumulation [9]. To better clarify the importance of (ii), let us consider the example of a through-thickness crack forming near one sensor. This crack would have a greater difference in waveform amplitude compared to a similar crack forming in the center of the specimen gage, whose waveforms propagate a similar distance. Using the maximum energy would imply that the crack that forms near one sensor creates more surface area than the crack that forms in the gage center; whereas, the average energy of these damage events would be similar, in correspondence with their similar crack areas. Prior to analysis, each AE event was manually checked for wave clipping (saturation), and no clipping was observed.

3. Results

Relating the total surface area created by all damage mechanisms (hereafter referred to as the damaged area) to the accumulated AE energy is currently prevented by limitations in resolving subsurface damage mechanisms. Here, the occurrence of visible matrix cracks on a specimen surface was used to estimate the damaged area up to matrix crack saturation. We assume from prior results [6,7] that there is a linear relationship between the accumulated surface area created by damage and the accumulated AE energy. This relationship is maintained if non-dominant mechanisms are captured by AE, as we assume these mechanisms occur simultaneously with the dominant damage mechanisms, although the strain energy released by these mechanisms is lower than that released by SiC fracture [7,8,10]. In recent work by the authors, a strong correlation was shown between the crack density evolution (CDE) estimated from AE energy accumulation and in-SEM measurements, with overestimates by the AE-predicted CDE (<5%) likely resulting from independently occurring secondary mechanisms [7]. Here, we neglect the small contribution from their possible independent occurrence but consider the possibility of their simultaneous occurrence with matrix cracking and fiber breaks.

3.1. Domain I: modeling damage progression up to matrix crack saturation

The cumulative AE energy up to matrix crack saturation (AE^T_{sat}) was calculated as the sum of the energies created by N events ($E(N)$) up to N_{sat} that preceded matrix crack saturation:

$$AE^T_{sat} = \sum_{N=1}^{N_{sat}} E(N) \quad (1)$$

In determining AE^T_{sat}, matrix crack saturation was taken as the point in the AE energy accumulation curve where a plateau or lull in activity was observed, as shown for SiC/SiC minicomposites in [11]. This occurred at a globally-applied stress of 700 MPa ± 100 MPa for the four LFC specimens and 900 ± 100 MPa for the four HFC specimens [7]. The total damage area at matrix crack saturation and its relationship to AE^T_{sat} is difficult to estimate. Some cracks do not propagate through-width, and some through-width cracks do not propagate normal to the loading direction. It is difficult to estimate the portion of debonded fibers along the plane of a crack due to a non-uniform fiber distribution [7]. The slip zone length also varies with local stress, and thus likely varies along the gage [12]. Currently, experimental capabilities are unable to visually observe all of these activities in the specimen bulk. Therefore, certain simplifying assumptions on specimen geometry and damage progression are made here in order to relate AE signals to the activity of damage mechanisms and creation of damaged surfaces.

In this work, we geometrically simplify each minicomposite as a cylinder with uniform fiber distribution and no porosity. We estimate the radius of the circular cross-section (R) by relating πR^2 to the average cross-sectional area (A_c) calculated using [8] and tabulated in Table 1.

We estimate the damage surface area that accumulates *prior* to

Table 1
Minicomposite properties.

Specimen ID	V_f (%)	V_i (%)	V_m (%)	Area (mm^2)	Γ (J/m^2)	τ (MPa)
HFC -1	37.93	25.87	36.20	0.170	5.5 ± 3.9	34.5 ± 13.0
HFC-2	39.58	26.99	33.43	0.163	5.5 ± 3.9	34.5 ± 13.0
HFC-3	39.65	27.03	33.32	0.162	5.5 ± 3.9	34.5 ± 13.0
HFC-4	44.07	25.88	30.05	0.146	5.5 ± 3.9	34.5 ± 13.0
LFC-1	26.96	2.59	70.43	0.239	1.2 ± 0.5	18.1 ± 4.8
LFC-2	28.12	2.70	69.18	0.229	1.2 ± 0.5	18.1 ± 4.8
LFC-3	30.67	2.94	66.39	0.210	1.2 ± 0.5	18.1 ± 4.8
LFC-4	28.66	2.75	68.58	0.224	1.2 ± 0.5	18.1 ± 4.8

matrix crack saturation as it relates to the accumulated AE energy, using both a lower and upper bound assumption:

1 **Lower Bound:** Cracks initiate in the matrix and deflect around fiber surfaces, with subsequent fiber debonding and sliding in the vicinity of each crack plane. Each crack creates two surfaces (i.e. crack faces) such that the accumulated area is the sum of the estimated areas of these surfaces.
2 **Upper Bound:** Cracks initiate in the matrix, leading to debonding of fibers from the interphase and sliding over some averaged length (l_m) in the cross-sectional area propagated by the crack. In addition to the two surfaces created by each crack, two surfaces are created by the slip zones on each side of the crack plane.

In the following section, we build a framework to assess the relationship between the AE energy at matrix crack saturation (AE^T_{sat}) and the corresponding damage area in each of these two cases.

3.1.1. Lower bound: matrix cracking

We take A_m to represent the average surface area created by a through-thickness transverse matrix crack that deflects around all fibers with no debonding:

$$A_m = 2 \bullet V_m \bullet A_c \tag{2}$$

where V_m is the matrix volume fraction, A_c is the specimen cross-sectional area, and the factor of two accounts for the formation of two crack faces (Table 1). As BN interphases are compliant relative to the matrix (elastic modulus ~20 GPa vs ~410 GPa for SiC [13,14]), we assume that the AE contribution of BN fracture was negligible to that of SiC cracking. Based on A_m, the total area generated by through-thickness matrix cracks (A^{tt}_m) is calculated as:

$$A^{tt}_m = A_m \bullet n_{tt} \tag{3}$$

where n_{tt} is the number of through-thickness cracks.

We also consider the areas created by cracks that have partially propagated through-width at matrix crack saturation, as these generate AE. We assume that the surface progression of a crack reflects it through-thickness progression. In Fig. 1, the sample shown in Fig. 1a (Orientation 1) is rotated to obtain the view shown in Fig. 1b (Orientation 2); the crack initially observed as partial-width now appears nearly through-width. The in-SEM view of minicomposite systems was susceptible to this orientation-dependent crack area measurement. Partial cracks made up 15 % of all cracks observed in-SEM at matrix crack saturation. It is possible that some cracks which appeared to be through-width, and are thereby assumed to be through-thickness, are also orientation-dependent partial cracks. We assume that the different possible sample rotations have an averaging effect, which is reasonable given that these minicomposites were not designed with any orientation-dependent anisotropy. For a partial crack of length l (Fig. 1a), we calculate the crack area ($A(l)$) as the area of the arc ABC (A_{ABC}) multiplied by V_m, which is the portion of the crack front surface area containing matrix. We compute A_{ABC} as:

$$A_{ABC} = \frac{R^2\theta}{2} - R\sin\left(\frac{\theta}{2}\right)(R - l) \tag{4}$$

$$\theta = 2\cos^{-1}\left(\frac{R - l}{R}\right) \tag{5}$$

where R is the radius of the sample cross-section, and θ is the angle swept out by the arc ABC in radians (Fig. 1). We calculate the matrix crack surface area $A(l)$ as:

$$A(l) = 2 \bullet V_m \bullet R^2 \left(\cos^{-1}(1 - x) - x(1 - x)\sqrt{\frac{2}{x} - 1}\right) \tag{6}$$

where $x = l/R$. The lower boundary on total surface area generated by cracks at matrix crack saturation (A^{lower}_{sat}) is calculated as the sum of the surface areas created by each through-thickness crack plus the surface areas created by p partially through-width cracks, each with an individual length l:

$$A^{lower}_{sat} = A^{tt}_m + \sum_{i=1}^{p} A(l_i) \tag{7}$$

The value of A^{lower}_{sat} was calculated for each specimen. The relationship between A^{lower}_{sat} and the AE energy accumulated up to matrix crack saturation (AE^T_{sat}) is then determined based on a coefficient for the AE energy per unit area released from matrix cracking (λ^c):

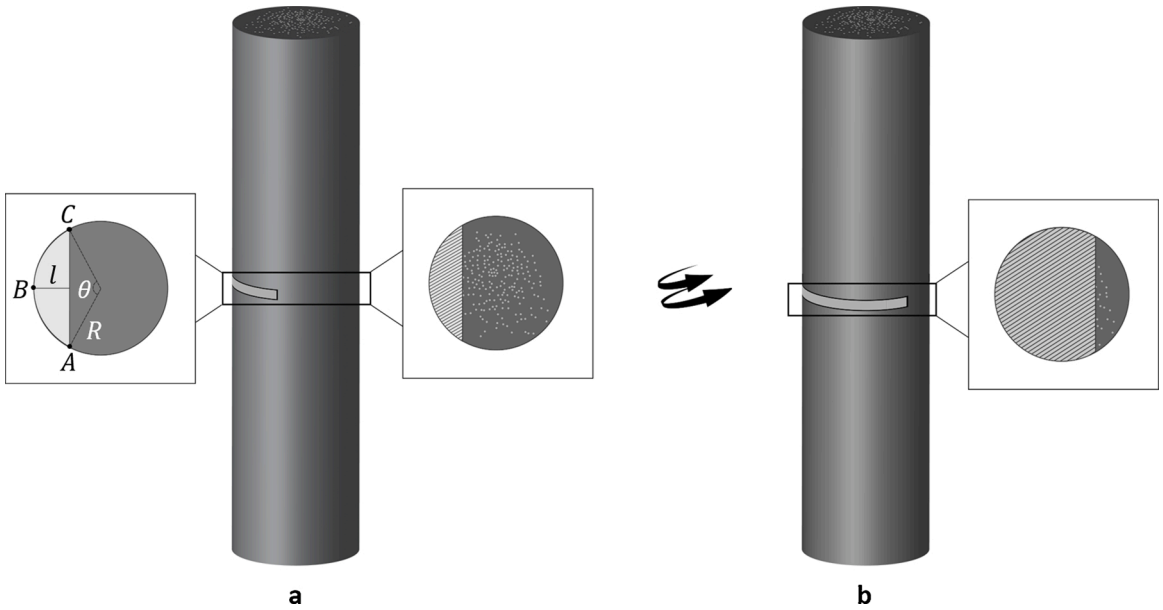

Fig. 1. a) Schematic of the minicomposite cross-section showing a partially through-width propagated crack (Orientation 1). In **b)** the sample is rotated such that the partially through-width crack appears as nearly through-width (Orientation 2).

$$AE_{sat}^{T} = \lambda^{c} \bullet A_{sat}^{lower} \quad (8)$$

The variable λ^c was calculated for each specimen and varied between 9.1-27.1 V^2•μs/mm^2 and 4.5-23.7 V^2•μs /mm^2 for the LFC and HFC specimens, respectively. At matrix crack saturation, nearly twice the AE energy was accumulated in LFC (62 V^2•μs – 218 V^2•μs) compared to HFC specimens (21 V^2•μs -118 V^2•μs). This increase can be attributed to the greater damaged surface area created by matrix cracking in the LFC specimens at this point, with lower bounds of ~6.74 mm^2 and ~3.98 mm^2 for LFC and HFC specimens, respectively. Using the λ^c parameter, Eq. 8 was modified:

$$A^{lower}(N) = \frac{E(N)}{\lambda^{c}} \quad (9)$$

where $A^{lower}(N)$ is the calculated area of event N and $E(N)$ is the AE energy of that event. The estimated damaged area created by each AE event up to the matrix crack saturation stress based on the lower bound is shown in Fig. 2.

3.1.2. Upper bound: matrix cracking with fiber debonding and sliding

The upper bound assumes that the surface area of an AE event is due to simultaneous matrix cracking, interfacial debonding, and sliding in the vicinity of the crack plane. We estimate the slip zone length using [15]: $l_m = \frac{(1-V_f)r\sigma}{2V_f\tau}$, where r is the fiber radius and τ is the interfacial shear stress, which are given for these minicomposite systems in [7]. For LFC specimens, the calculated l_m results in overlapping slip zones at the matrix crack saturation stress, indicating fully-debonded interphases. We therefore assume $l_m \approx 200$ μm, which is half of the matrix crack spacing calculated from the matrix crack densities in [7]. We assume that $l_m = l_d = l_s$, where l_d and l_s are the fiber debond and sliding lengths respectively, as the slip zone encompasses the region of interfacial debonding and frictional sliding. For HFC specimens, we do not assume the interface has fully debonded at matrix crack saturation. This is a non-standard material where models that consider thin, weakly-bonded interphases are not applicable. High interfacial shear stresses resist frictional sliding and slip zone extension once cracks are formed [16]. Moreover, l_m predicted assuming fully-debonded interphases (by way of crack density) exceeds the fiber pull-out lengths (Fig. 3) by 2x,

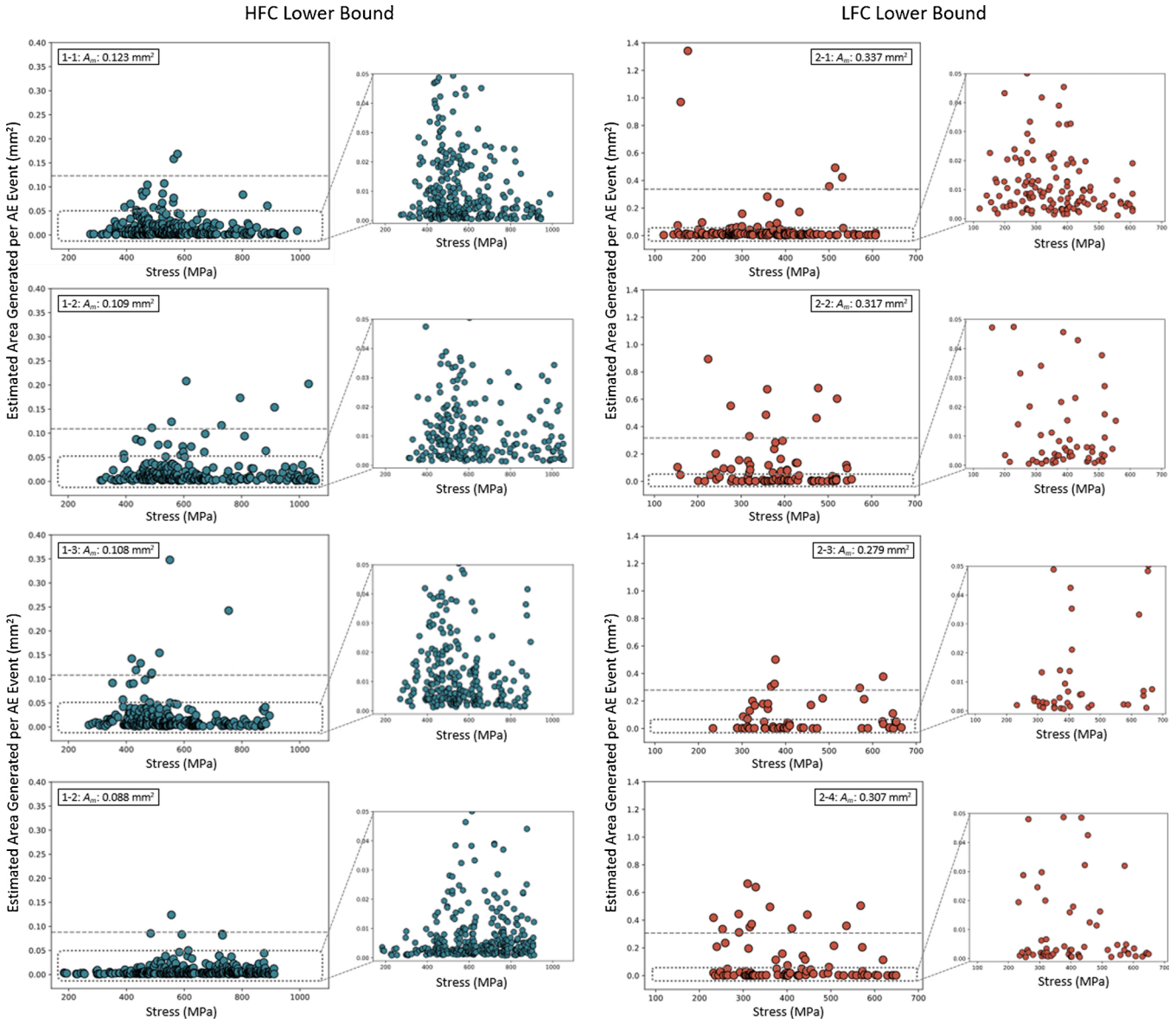

Fig. 2. The distribution in surface areas created per AE event of four HFC and four LFC specimens, mapped as a function of globally-applied stress based on the lower bound conditions, which underrepresents the damage areas.

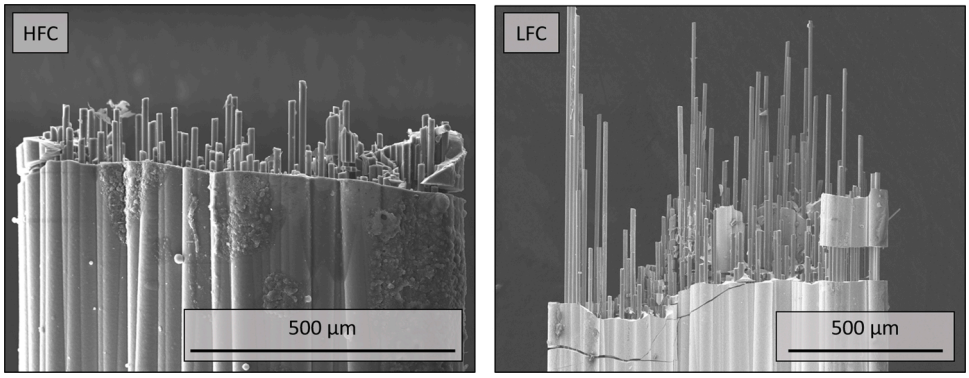

Fig. 3. HFC and LFC specimen fracture surfaces showing fiber-pullout, with fibers debonded from their interphases.

contradicting modeling results from Curtin [17]. To quantify the length over which fibers have debonded and slid, we use the following calculation from Goldberg et al. [18]:

$$l_m = \frac{r}{2\tau}\left(\sigma\frac{V_m E_m}{V_f E_c} - \sigma_f^T - \sigma_{deb}\right) \tag{10}$$

where σ_f^T is the thermal residual stress on the fiber, σ_{deb} is the critical debond stress, and σ is the applied stress (considered here as the matrix crack saturation stress, $\sigma = \sigma_{sat}$). The matrix volume fraction (V_m) includes the volume fraction of interphase, as it has been shown experimentally [7,19] that debonding primarily occurs at the fiber-interphase surface. The composite modulus (E_c) is calculated following a rule-of-mixtures of the matrix and fibers, and the critical debonding stress (σ_{deb}) is calculated following Hutchinson and Jensen [12]. We calculate the thermal residual stress (σ_f^T) following Chulya et al. [20]. From Eq. 10, l_m for HFC specimens is ≈80 μm, which will later be used to compute the slip zone area.

To estimate the area contributions of interfacial debonding and sliding, we first approximate these for a single through-thickness crack. Assuming all fibers debond and slide by l_m along the crack plane ($l_m = l_d = l_s$) at matrix crack saturation, we calculate the slip zone *area* along the crack plane ($A_{tt}^{l_m}$) as the fiber circumference ($2\pi r$) multiplied by the slip zone length (l_m) and the number of fibers in the tow ($n_{FT} = 500$):

$$A_{tt}^{l_m} = 2(2\pi r l_m \bullet \mathrm{n_{FT}}) \tag{11}$$

where the factor of two accounts for the slip zone area on both sides of the crack.

In the plane of a partial-width crack, we assume that the surface progression of the crack reflects its through-thickness progression. We also assume the fraction of fibers debonded and slid reflects the specimen's global volume fractions (i.e. uniformly distributed fibers). At matrix crack saturation, we assume the slip zone length of the partially cracked region is also l_m. We expect slip to occur adjacent to each crack in identical fashion, such that l_m is the same for all cracks at a fixed stress. For a crack of length l (Fig. 1a), we calculate the fiber area within the crack front surface area by multiplying the area of arc ABC (Eqs. 4 and 5) by the fiber volume fraction (V_f):

$$A_f(l) = V_f R^2\left(\cos^{-1}(1-x) - x(1-x)\sqrt{\frac{2}{x}-1}\right) \tag{12}$$

where $x = l/R$. The number of fibers in the partial-width crack wake ($n_f(l)$) can be estimated as the area of the fibers calculated in Eq. 12 divided by the surface area of the circular fiber cross-section (πr^2):

$$n_f(l) = \frac{A_f(l)}{\pi r^2} \tag{13}$$

The fiber debond area in the partial-width crack wake at matrix crack saturation ($A^{l_m}(l)$) is:

$$A^{l_m}(l) = 2(2\pi r l_m \bullet \mathrm{n_f(l)}) \tag{14}$$

where the factor of two accounts for the slip zone area on both sides of the matrix crack. The total slip zone area generated at matrix crack saturation ($A_{sat}^{l_m}$) is the sum of the slip zone areas along the plane of all through-thickness cracks (n_{tt}) (Eq. 11) plus the sum of the slip zone areas along the plane of p partial-width cracks (Eq. 14), each of an individual crack length l:

$$A_{sat}^{l_m} = n_{tt} \bullet \mathrm{A_{tt}^{l_m}} + \sum_{i=1}^{p} \mathrm{A^{l_m}(l_i)} \tag{15}$$

where $A_{sat}^{l_m}$ is equivalent to the areas of the debonded ($l_m = l_d$) and slid region ($l_m = l_s$).

The upper bound estimate of the *total* damage area generated at matrix crack saturation is then:

$$A_{sat}^{upper} = A_{sat}^{lower} + A_{sat}^{l_d} + A_{sat}^{l_s} \tag{16}$$

where the area of interfacial debonding and sliding are equivalent but are considered separately.

The relationship between the AE energy accumulated up to matrix crack saturation (AE_{sat}^T) and the surface area created using the upper bound calculation is:

$$AE_{sat}^T = \lambda^c \bullet \mathrm{A_{sat}^{lower}} + \lambda^d \bullet \mathrm{A_{sat}^{l_d}} + \lambda^s \bullet \mathrm{A_{sat}^{l_s}} \tag{17}$$

where λ^d is the specimen-dependent coefficient for AE energy per unit area released from fiber debonding, and λ^s is the specimen-dependent parameter for AE energy per unit area released from sliding. We consider these separately, as the strain energy released by each mechanism will vary (i.e. we expect that debonding is "louder" than sliding). It is infeasible to directly quantify λ^d and λ^s, as it is currently not possible to decouple interfacial AE events from bulk AE. We instead indirectly quantify λ^d by assuming that the ratio of AE energy released per unit area of SiC cracking versus that per unit area of fiber debonding equals the ratio of the strain energy release rates of the two mechanisms. For CVI SiC, the strain energy release rate, $\Gamma_m \approx 14.1$ J/m^2 [8]. For debonding, we use the average interface debond toughness, with $\Gamma = 1.2$ J/m^2 and $\Gamma = 5.5$ J/m^2 for LFC and HFC specimens, respectively (Table 1) [7]. We indirectly quantify λ^s, assuming that the ratio between the λ terms for fiber sliding and the matrix cracking is equivalent to the ratio of the interfacial shear stress (τ) and the matrix cracking stress (σ_{cr}^m), which has previously been quantified by Almansour et al. [8]. Eq. 17 can then be rewritten as:

$$AE_{sat}^T = \lambda^c \bullet \mathrm{A_{sat}^{lower}} + \left(\lambda^c \bullet \frac{\Gamma}{\Gamma_m}\right) \bullet \mathrm{A_{sat}^{l_d}} + \left(\lambda^c \bullet \frac{\tau}{\sigma_{cr}^m}\right) \bullet \mathrm{A_{sat}^{l_s}} \tag{18}$$

where λ^d and λ^s are now estimated in terms of λ^c. This parameter can be pulled out in Eq. 19 to relate AE^T_{sat} to the specimen-dependent parameter, which captures the AE energy released from the matrix cracking, fiber debonding, and sliding. For this reason, we replace the λ^c term with $\lambda^{c,d,s}$:

$$AE^T_{sat} = \lambda^{c,d,s} \bullet \left(A^{lower}_{sat} + \frac{\Gamma}{\Gamma_m} \bullet A^{l_d}_{sat} + \frac{\tau}{\sigma^m_{cr}} \bullet A^{l_s}_{sat}\right) \quad (19)$$

The variable $\lambda^{c,d,s}$ varied between 1.5–4.2 $V^2 \bullet \mu s/mm^2$ and 0.3–1.8 $V^2 \bullet \mu s/mm^2$ for LFC and HFC specimens, respectively. The surface area created by each AE event N based on the upper bound $A^{upper}(N)$ up to the matrix crack saturation stress is calculated as:

$$A^{upper}(N) = \frac{E(N)}{\lambda^{c,d,s}} \quad (20)$$

3.1.3. Comparison of lower and upper bound surface area estimates

The estimated surface areas created by each AE event are shown in Figs. 2 and 4 for the lower and upper bound, respectively. The surface area of an average through-thickness matrix crack (A_m) is labeled in each plot and shown as a dashed line on the y-axis. A_m was larger in LFC versus HFC specimens, due to their ~ 40 % larger cross-sections and 100 % larger matrix volume fractions compared to HFC specimens.

LFC specimens generated fewer AE events under tension than similarly sized HFC specimens; thereby, on average, individual events tended to create larger surface areas. Assuming only matrix cracking (lower bound), 2% of HFC events prior to matrix crack saturation had surface areas exceeding A_m versus ~5% of LFC events (Fig. 2). In HFC specimens, <50 % of such large area AE events exceeded 120 % A_m. In contrast, ~65 % of such AE events in LFC specimens exceeded 120 % of A_m. This observation is corroborated by prior findings that *larger*, through-thickness cracks formed in *fewer* stages in LFC specimens versus HFC specimens [7]. The estimates of constituent volume fractions and cross-sectional area made in Table 1 (using [8]), rely on weighted averages. However, in-SEM observations indicate differences in matrix volume content (variations in specimen width along the gage in 40−50 μm were common); here, we use 120 % of A_m as an upper bound approximation of matrix volume fraction in any local area. As such, AE events corresponding to areas between A_m and 120 % of A_m may be the result of through-thickness cracking at positions with higher local

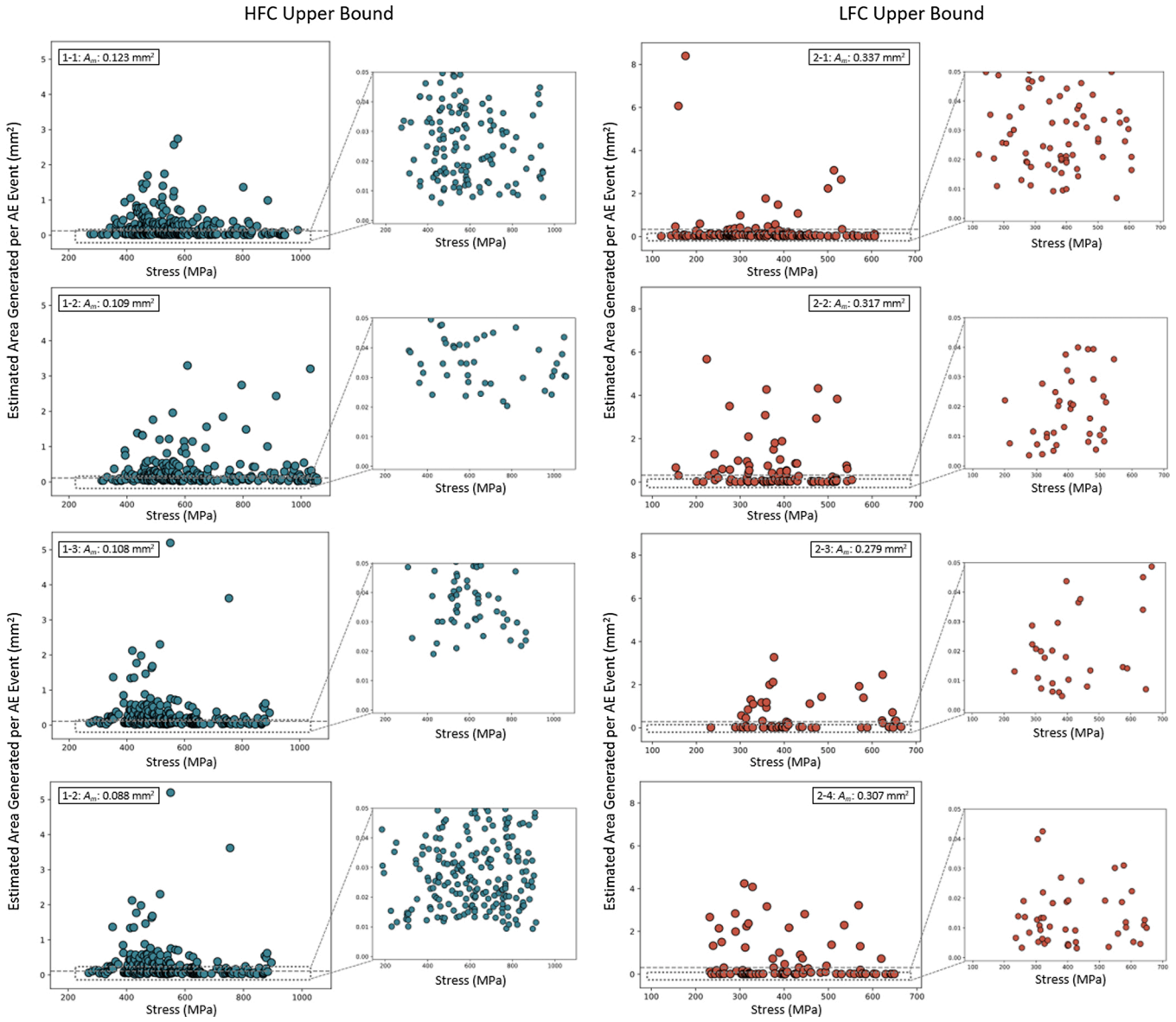

Fig. 4. The distribution in surface areas created per AE event in four HFC and four LFC specimens, mapped as a function of globally-applied stress based on the upper bound conditions, which likely overrepresents the damage areas.

matrix content (and correspondingly, lower matrix content for events with estimated size between A_m and 80 % of A_m).

The smallest AE events (~0.0005 mm^2 and ~0.0008 mm^2 for LFC and HFC specimens, respectively), displayed as insets in Fig. 2, indicate that the lower bound under-represented the surface areas created by damage events. If AE was only sensitive to the matrix cracking, one would expect larger crack areas in LFC specimens, as their higher matrix content and 'continuous' matrix microstructure created a more coherent in-plane pathway for crack propagation [7]. Additionally, the smallest AE events are on the order of the surface area created by a few fiber breaks. If one considers the average matrix crack area A_m in terms of fiber size, by dividing A_m by the surface area created by a single fiber break, A_m is equivalent to ~400 and ~1100 fiber breaks in HFC and LFC specimens, respectively. While early fiber breaks have been observed in CMCs prior to matrix crack saturation [6] and potentially account for some of these small AE events, it is unlikely that a significant number of matrix cracks would propagate to create areas on the order of a few fibers. These trends motivate the consideration of secondary mechanisms.

Using the upper bound condition, the calculated surface areas of AE events in LFC specimens exceeded were ~6x larger than their lower bound estimates. The estimated surfaces areas of HFC specimens were much larger, at ~15x the lower bound estimates, mainly due to the high debond toughness (nearly 5x that of LFC specimens). The largest areas estimated by the upper bound were ~20x the average through-thickness matrix crack (A_m) in LFC specimens and ~40x of A_m in HFC specimens. Some events whose calculated surface areas exceeded A_m were a result of simultaneous cracking, debonding, and sliding, following upper bound assumptions. In an analogous approach to Eq. 19, we estimate the formation area of an average through-thickness crack whose slip zone extends to its maximum:

$$A_{max}^{upper} = A_m + \frac{\Gamma}{\Gamma_m} A_{sat}^{l_d} + \frac{\tau}{\sigma_{cr}^m} A_{sat}^{l_s} \tag{21}$$

Using the area estimates for the slip zone region (Eq. 11) for the debonding and sliding area, the maximum for a single through-thickness crack is calculated as ~6–7x of A_m in LFC specimens and ~9–10x of A_m in HFC specimens. While this accommodates most AE events larger than A_m, there are still events that exceed even these limits. One possibility is that these events reflect multiple matrix crack formation, where near-simultaneous cracking within a small timeframe amplifies a waveform's energy. However, more AE events with areas significantly exceeding A_m were observed in HFC versus LFC specimens. As HFC specimens exhibited smaller crack and slip zone areas than LFC specimens, these results indicate that the upper bound overestimated the size of AE events.

The lower bound, i.e. the assumption that only matrix cracking can be captured by AE, is used to explore the sensitivity of AE to secondary mechanisms. By this assumption, we find frequently occurring events that correspond to crack areas on the order of a few fiber breaks. It is unlikely, especially for the LFC microstructure [7], that a significant portion of matrix cracking AE events would occur in such small propagation steps. Rather, these small events may be from secondary mechanisms that release lower strain energies and create smaller surface areas, indicating that AE is sensitive to such mechanisms even when they occur simultaneously with the dominant damage mechanism. It is assumed here that AE is sensitive either to the matrix cracking mechanism or is sensitive enough to capture matrix cracking and simultaneously occurring interfacial phenomena. However, these mechanisms may act independently to generate AE. Future work will aim to either distinguish these mechanisms or verify their simultaneous occurrence and include factors such as variations in the slip zone length, non-uniform fiber distribution, and representative geometries of the minicomposite cross-section and volume into modeling the damaged area. It is likely that an accurate measure of the accumulated damage lies in the envelope between the two bounds discussed here.

3.2. Domain II: modeling damage progression beyond matrix crack saturation

The surface areas created by AE events beyond matrix crack saturation were estimated based on the lower bound of Section 3.1 for each specimen ($A^{lower}(N)$) were calculated as:

$$A^{lower}(N) = \frac{E(N)_{N>Nsat}}{\frac{\Gamma_f}{\Gamma_m}\lambda^c} \tag{22}$$

We consider the effect of varying fracture toughness between the CVI SiC (reported as 14.1 J/m^2 [8]) and the HNS fibers (calculated as 10.2 J/m^2 from values reported in [21]). The same values for λ^c are utilized as we assume AE is only sensitive to the dominant damage mechanisms in this scenario. The lower bound on the total damage area generated up to failure (A_T^{lower}) was calculated as the sum of the areas created by all AE events, where N_f is the event at failure:

$$A_T^{lower} = \sum_{N=1}^{N_f} A^{lower}(N) \tag{23}$$

Based on the upper bound of Section 3.1, we calculate that fibers are fully debonded in LFC specimens and partially debonded in HFC specimens at matrix crack saturation. In Domain II, fiber breaks are accompanied by sliding adjacent to each break, and we derive a relationship similar to Eq. 3.18 for the active mechanisms. Unlike in Domain I, it is infeasible to estimate the areas created in Domain II, as we cannot directly measure the number of fiber breaks. However, we can indirectly find the relationship *up to* matrix crack saturation for the two mechanisms active *beyond* this state (SiC cracking and fiber sliding), and apply that estimate to events in Domain II:

$$AE_{sat}^T = \frac{\Gamma_f}{\Gamma_m}\lambda^c \bullet \mathrm{A}_{\mathrm{sat}}^{\mathrm{lower}} + \left(\lambda^{\mathrm{c}} \bullet \frac{\tau}{\sigma_{\mathrm{cr}}^{\mathrm{f}}}\right) \bullet \mathrm{A}_{\mathrm{sat}}^{\mathrm{l_f}} \tag{24}$$

We assume that the ratio of the strain energy release rates between fiber sliding and fracture is equivalent to the ratio of the interfacial shear stress and the critical fiber cracking stress (σ_{cr}^f). Callaway et al. [22] found strengths of ~2.0 GPa for lubricated bundles of HNS fibers, which we use here for the critical fiber cracking stress. We calculate the sliding zone area at matrix crack saturation ($A_{sat}^{l_s}$), considering the sliding length of fibers once they are broken. For LFC specimens, based on modeling by Curtin [4], we calculate the sliding length adjacent to a fiber break (l_f) as:

$$l_f = \frac{r\sigma}{2\tau} \tag{25}$$

where we consider σ to be the stress at rupture to estimate the maximum fiber sliding length. This is approximately 160 μm for LFC specimens (or 80 % of the sliding zone length estimated in Domain I). For HFC specimens, we consider that the sliding zone length of a fiber after fracture is inferior to the slip zone length (l_s =80 μm) found in Domain I. We assume there is no slip zone extension beyond matrix crack saturation. This is due to both high interfacial parameters that inhibit slip zone extension and the mitigation of stresses at the interface by fiber fracture within the debonded region around cracks. The fiber sliding lengths are taken to be shorter than the slip length l_m in HFC specimens as well, given their higher interfacial shear stress and partially bonded interface; we therefore approximate in HFC specimens that $l_f \approx 80$ % of l_s, or $l_f \approx 65$ μm. We apply these values to compute the sliding zone area following Eqs. 10–15, again considering the difference in contribution per unit area between the fiber breakage and frictional sliding. We factorize the λ^c term of Eq. 24, and the resultant Eq. 26 is now related to the area created by both the fiber breakage and the frictional sliding. For clarity, we rename λ^c as $\lambda^{c,s}$:

$$AE_{sat}^T = \lambda^{c,s} \bullet \left(\frac{\Gamma_{\mathrm{f}}}{\Gamma_{\mathrm{m}}} \bullet \mathrm{A}_{\mathrm{sat}}^{\mathrm{lower}} + \frac{\tau}{\sigma_{\mathrm{cr}}^{\mathrm{f}}} \bullet \mathrm{A}_{\mathrm{sat}}^{\mathrm{l_f}}\right) \tag{26}$$

We find that $\lambda^{c,s}$ varied between 10.1 - 24.0 V^2 μs/mm^2 and 4.3 - 21.0 V^2 μs/mm^2 for LFC and HFC specimens, respectively. The surface area created by each AE event N based on the upper bound ($A^{upper}(N)$) *beyond* the matrix crack saturation stress is calculated as:

$$A^{upper}(N) = \frac{E(N)_{N>Nsat}}{\lambda^{c,s}} \tag{27}$$

However, it is not particularly useful to estimate accumulated damage in Domain II in terms of surface area alone. Rather, we now consider the following two conditions to describe the damage evolution captured by AE between the matrix crack saturation stress failure to contextualize these areas in terms of the fiber break evolution:

Condition 1: Based on the lower bound (Section 3.1), AE events are only produced by fiber breaks beyond matrix crack saturation. We assume that each break produces an area A_f such that:

$$A_f = 2\pi r^2 = 0.00027 mm^2 \tag{28}$$

where the fiber radius r ~6.5 μm and two surfaces are created when a fiber breaks. We estimate the number of fiber breaks corresponding to

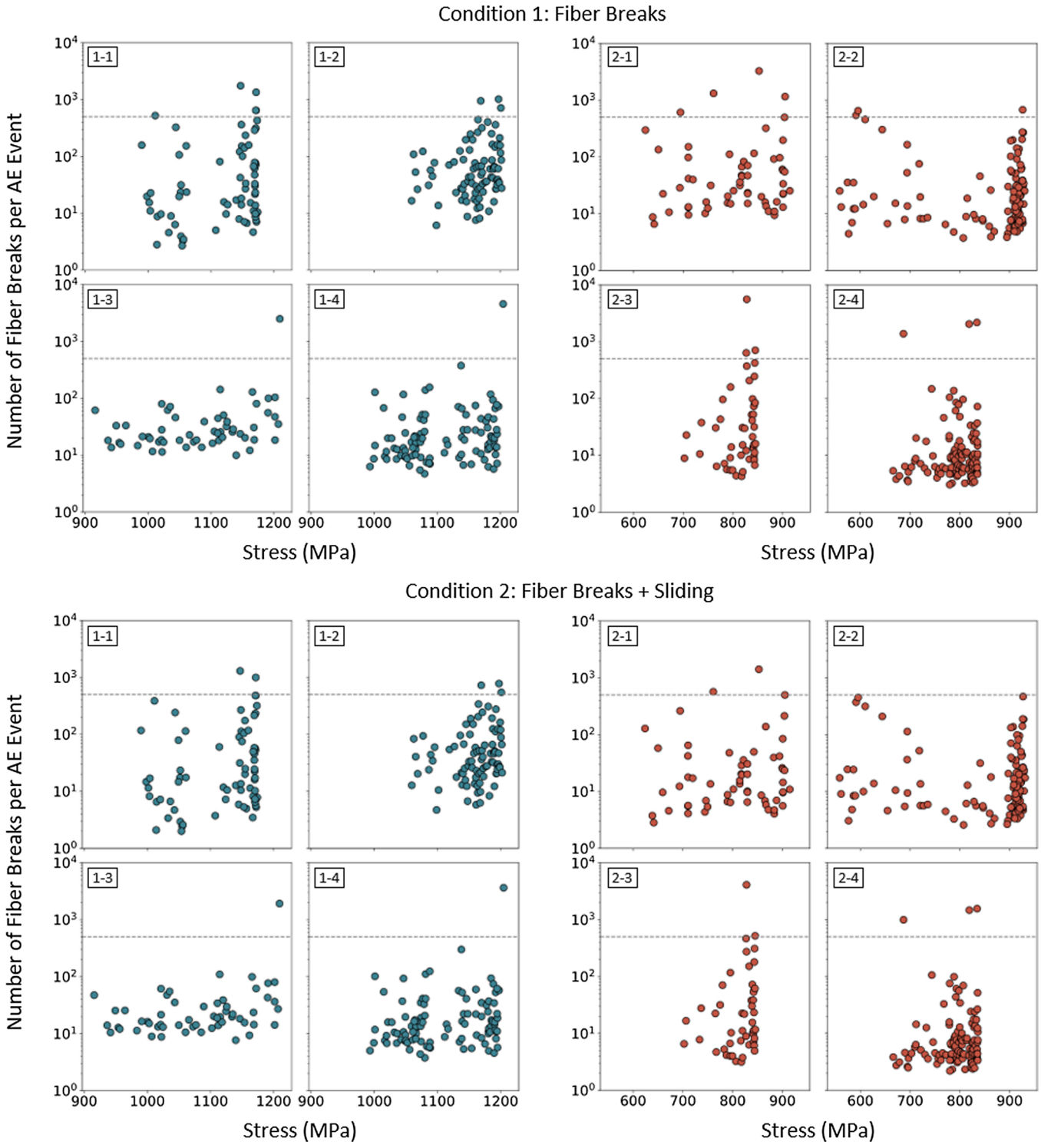

Fig. 5. Estimated number of fiber breaks per AE event for all specimens by Conditions 1 and 2.

the area of each AE event as:

$$N_{f,}^{lower} = \frac{A_{N>N_{sat}}^{N(lower)}}{A_f} \quad (29)$$

Condition 2: Based on the upper bound (Section 3.1), we assume AE events beyond matrix crack saturation capture the energies produced by both fiber breaks and subsequent frictional sliding, where the area created by a single fiber break is:

$$A_f = 2\pi r^2 + 2(2\pi r l_f) \quad (30)$$

The first term accounts for the two fracture surfaces created by the fiber break, and the second term accounts for the slip zone area on both sides of the fiber break as it pulls out. We approximate the number of fiber breaks created by each AE event:

$$N_f^{upper} = \frac{A_{N>N_{sat}}^{N(upper)}}{\frac{\Gamma_f}{\Gamma_m}2\pi r^2 + \frac{\tau}{\sigma_{cr}^f}2(2\pi r l_f)} \quad (31)$$

We consider the effect of the varying strain energy release rates in Eq. 31, as was done in Section 3.1 for the upper bound. This is because the sliding area created around a fiber is an order of magnitude larger than the surface area created by the break itself, while the strain energy released by the event is not. With these conditions, the damaged area created beyond matrix crack saturation can be calculated for each specimen in terms of the number of fiber breaks.

3.2.1. Comparison of fiber break distribution estimates

The trends observed at all conditions indicate that most AE events beyond matrix crack saturation are small relative to the size of the AE event(s) generated at failure. This finding is consistent with the current understanding of how fiber bundles fail [17,23–25]. Often, failure occurred not at the ultimate tensile stress (UTS), but upon further applied displacement that led to a cascade of fiber breaks, resulting in a slightly lower stress prior to the full tow rupture. The evolution of fiber breaks per AE event as a function of stress is shown in Fig. 5 for Conditions 1 and 2 described above. We find that most AE events are generated by fiber breaks occurring in small quantities prior to tow rupture. The dashed horizontal line in each sub-figure represents the fiber tow size (500 fibers).

Over 500 fiber breaks were predicted for all specimens at both conditions, in agreement with [26], who found that fibers failed more than once by sliding to recover previously carried stress, and estimated a total fiber break count of ~750 fiber breaks per specimen via x-ray microtomography (μCT). The specimens in [26] had the same fiber type and number of fibers as in this work, with different interfacial properties. The fiber break count of [26] should be considered a lower bound due to the potential for undetected fiber breaks, such as from the μCT resolution of ~1 μm. The work of [26] indicated that fibers may break multiple times near the fracture zone, as a decay in fiber break density was observed away from the fracture plane; these breaks would be difficult to capture due to the spatial and temporal resolution limitations of current experimental capabilities. For all specimens, we find at minimum one event corresponding to a fiber fracture estimate exceeding the tow size. We would expect this given that at the rupture state, broken fibers can rapidly be reloaded and break again [26,27], potentially in the time window of a single AE event.

For Condition 1, where it was assumed that AE was only sensitive to fiber fracture, we estimate a higher fiber break count, with ~8200 (~16 breaks/fiber) and ~7800 (~15 breaks/fiber) fiber breaks in LFC and HFC specimens, respectively. For Condition 2, where it was assumed that AE was sensitive to the occurrence of fiber breaks and subsequent sliding, we estimate ~5200 (~10 breaks/fiber) and ~5900 (~12 breaks/fiber) in LFC and HFC specimens, respectively.

It is useful to compare the outcomes of the aforementioned conditions to modeling predictions of the total number of fiber breaks at the UTS. Curtin [4] approximated the fraction of broken fibers in the wake of a crack at the UTS as: $q = 2/(m+2)$, where m is the Weibull modulus describing the variability in fiber strengths. From [4], the total number of fibers broken can be estimated as:

$$f_{broken} = (q \bullet n_c + (1 - q)) \bullet n_{FT} \quad (32)$$

where $n_{FT} = 500$ fibers in the tow, and n_c refers to the total number of matrix cracks. The first term in Eq. 32 accounts for the portion of the fiber tow broken at each matrix crack prior to composite failure, and the second term accounts for the portion of unbroken fibers at the failure location breaking the minicomposite rupture stress. For HNS fibers, there are reported measurements of the Weibull modulus in the range of $m = 4.49$–8.42 [22,28,29]. If we consider this range as bound for the q, we find $q = 0.19 - 0.31$. The total number of fibers broken at the UTS for LFC specimens is 3250–5000 fibers, and for HFC specimens as 4400–6800 fibers.

A primary conclusion is that AE is sensitive enough to capture the combined effects of dominant and non-dominant mechanisms. While Condition 1 overestimates the ranges predicted by [4], Condition 2 falls squarely within these ranges. Moreover, when a reasonable estimate of the accumulated damage area is determined, a predicted number of fiber breaks matching the micromechanics-predicted number of breaks results. As such, point-by-point AE data contains meaningful information indicative of both the damage mode and the size of that damage source. A small portion of fiber breaks do occur below the matrix crack saturation stress [6], which is not accounted for in this model.

While we only consider the activity of fiber breaks and sliding in Domain II, other mechanisms are active. Mixed-mode rupture events, where fragments of the matrix fractured when the tow failed (shown in Fig. 6), were often observed in-SEM. Fiber tow rupture in conjunction with this additional cracking would likely create the equivalent of >500 fiber fracture surfaces. As such, it is possible that pre-rupture AE events, which occur with estimated areas exceeding the tow size, also capture additional subsurface matrix cracking. Quantifying the areas created by this additional cracking, whether the damage mechanism is observed at the surface (as in Fig. 6) or at the subsurface, is infeasible by SEM measurements alone and requires further exploration.

One possible source of error to consider in future studies is waveform attenuation, which increases as damage accumulates, and is related to elastic material parameters, number of cracks, and the degree of crack opening [9,30,31]. Maillet et al. [30] found an increase in peak frequencies and frequency centroids with stress, which may indicate the transition between a matrix cracking vs. fiber break dominated response. It is unclear whether this increase in frequency characteristics is due to increased signal attenuation with accumulated damage, or whether damage mechanisms at higher stresses (i.e. fiber breaks) have higher characteristic frequencies. This is because the frequency characteristics of an event, which are related to the stored strain energy released by its occurrence, may be mechanism independent. Let us consider the example of two fibers breaking at different strains that create equivalent surface areas. The fiber break at higher strains has more stored strain energy but its released signal is more damped than the fiber break at lower strains, as its AE must propagate through a greater amount of accumulated damage. The degree to which these competing mechanisms offset or negate each other requires further study. However, their combined effect is likely minimized at lower strains, given the linear relationship between accumulated AE energy and damage area during the matrix cracking dominated response [6].

We did not measure signal attenuation, which relies on factors that are difficult to control (e.g. sensor coupling to specimens). Morscher et al. [9] used lead breaks to measure waveform propagation between sensors but found lead breaks to be inconsistent sources. Maillet et al. [31] studied variations in thousands of recorded waveforms in increments of time and space, in order to quantify the attenuation coefficient evolution. A method such as acousto-ultrasonics (AU), in which

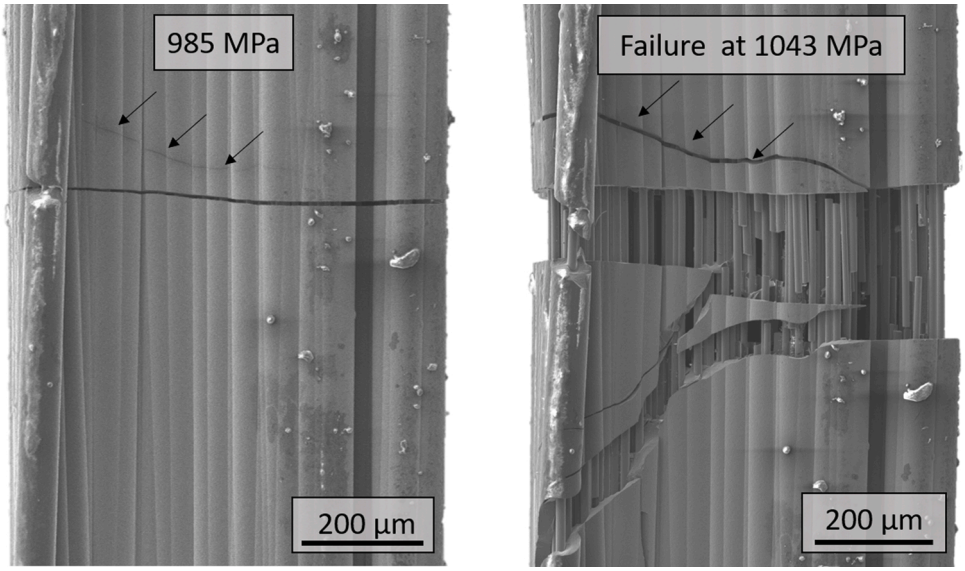

Fig. 6. Mixed-mode fracture events occurred with fiber tow rupture. The surfaces created by these events contributed to the energy of the rupture AE event but are infeasible to quantify.

artificial sources produce waveforms, could be leveraged in-SEM to quantify the initial signal loss and measure progressive attenuation. This approach has previously been used in conjunction with AE to study damage modes in CMCs [32]. Another potential source of error is the AE transducer sensitivity. Recent work by Guel et al. [33] shows that AE transducers with overlapping broadband frequency ranges vary in sensitivity to certain frequencies. As such, the AE data acquired using a single sensor type may be unable to detect certain frequency characteristics (and thereby a portion of the total energy) of the originating damage sources, leading to an underestimation of the damage accumulation. In such a scenario, the error can be mitigated using a similar approach to Guel et al., wherein two sensor types with varying frequency sensitivities are used to assess the damage accumulation [33].

4. Conclusions

The relationship between damage sources and their corresponding AE events in SiC/SiC minicomposites was modeled using insights gained from a combined approach of in-SEM tensile testing and AE measurements. Damage progression was estimated over two domains: Domain I, up to the matrix crack saturation; and Domain II, beyond matrix crack saturation. While prior efforts have assumed that only dominant damage mechanisms (matrix cracking and fiber failure) contribute AE, as they have higher strain energy rates than secondary mechanisms such as fiber debonding and sliding, we find that secondary mechanisms are also captured in AE.

We analyze Domain I using a lower and upper bound assumption: the lower bound assumes that AE is only sensitive to capturing matrix cracking, and the upper bound assumes that AE can capture the near-simultaneous occurrence of matrix cracking, fiber debonding, and fiber sliding in the vicinity of the crack plane. The lower bound resulted in unrealistically small crack areas in both LFC and HFC specimens, where the smallest AE events were on the order of the fracture area of a few fibers. We hypothesize that the smallest (lowest energy) AE events resulted from secondary mechanisms, which have lower strain energy release rates than the SiC cracking. The upper bound likely overestimated the areas created by matrix cracking and fiber debonding and sliding in the crack wake, in part due to over-estimations of the slip zone area, and the contribution estimates of the debonding mechanism relative to the matrix cracking.

In Domain II, we estimate the number of fiber breaks per AE event beyond matrix crack saturation by the following conditions: AE is sensitive to (i) only fiber fracture, and (ii) combined fiber fracture and fiber sliding. In all specimens, at least one AE event at rupture where the predicted number of fiber breaks exceeded the tow size was estimated. We find that Condition (i) overestimates fiber break evolution, while Condition (ii) estimates overlay well with the expected number of fiber breaks predicted by [4]. This finding indicates that AE is sensitive to both dominant and non-dominant damage mechanisms. However, further work is needed to characterize the AE energy density contributions of secondary mechanisms in order to more accurately map the damage accumulation.

Declaration of Competing Interest

The authors report no declarations of interest.

Acknowledgements

B. Swaminathan gratefully acknowledges financial support from NASA Space Technology Research Fellowship: (Grant: 80NSCC17K0084) and use of the NASA Glenn Research Center facilities. N. McCarthy, A. Musaffar, T. Pollock, and S. Daly gratefully acknowledge financial support from the National Science Foundation (Award: 1934641) as part of the HDR IDEAS^2 Institute. Material was provided by Rolls-Royce High Temperature Composites. We thank Mr. Pete Bonacuse and Dr. Wayne Jennings at NASA GRC for their assistance in electron microscopy, and Prof. Frank Zok at UCSB for his insights into the mechanics of CMCs.

References

[1] D.B. Marshall, B.N. Cox, A.G. Evans, The mechanics of matrix cracking in brittle-matrix fiber composites, Acta Mater. 33 (1985) 2013–2021.
[2] B.F. Sorenson, R. Talreja, Analysis of damage in a ceramic matrix composite, Int. J. Damage Mech. 2 (1993) 246–271.
[3] B. Budiansky, J.W. Hutchinson, A.G. Evans, Matrix fracture in fiber-reinforced ceramics, J. Mech. Phys. Solids 34 (1986) 167–189, https://doi.org/10.1016/0022-5096(86)90035-9.
[4] W.A. Curtin, Theory of mechanical properties of ceramic-matrix composites, J. Am. Ceram. Soc. 74 (1991) 2837–2845, https://doi.org/10.1111/j.1151-2916.1991.tb06852.x.
[5] G.N. Morscher, Modal acoustic emission of damage accumulation in a woven SiC/SiC composite, Compos. Sci. Technol. 59 (1999) 687–697, https://doi.org/10.1016/S0266-3538(98)00121-3.

[6] E. Maillet, A. Singhal, A. Hilmas, Y. Gao, Y. Zhou, G. Henson, G. Wilson, Combining in-situ synchrotron X-ray microtomography and acoustic emission to characterize damage evolution in ceramic matrix composites, J. Eur. Ceram. Soc. 39 (2019) 3546–3556, https://doi.org/10.1016/j.jeurceramsoc.2019.05.027.
[7] B. Swaminathan, N.R. McCarthy, A.S. Almansour, K. Sevener, T.M. Pollock, J. D. Kiser, S. Daly, Microscale characterization of damage accumulation in CMCs, J. Eur. Ceram. Soc. 41 (May (5)) (2021) 3082–3093, https://doi.org/10.1016/j.jeurceramsoc.2020.05.077.
[8] A. Almansour, E. Maillet, S. Ramasamy, G.N. Morscher, Effect of fiber content on single tow SiC minicomposite mechanical and damage properties using acoustic emission, J. Eur. Ceram. Soc. 35 (2015) 3389–3399, https://doi.org/10.1016/j.jeurceramsoc.2015.06.001.
[9] G.N. Morscher, A.L. Gyekenyesi, The velocity and attenuation of acoustic emission waves in SiC/SiC composites loaded in tension, Compos. Sci. Technol. 62 (2002) 1171–1180, https://doi.org/10.1016/S0266-3538(02)00065-9.
[10] S. Bertrand, P. Forio, R. Pailler, J. Lamon, Hi-Nicalon/SiC minicomposites with (pyrocarbon/SiC)$_n$ nanoscale multilayered interphases, J. Am. Ceram. Soc. 82 (1999) 2465–2473, https://doi.org/10.1111/j.1151-2916.1999.tb02105.x.
[11] N. Lissart, J. Lamon, Damage and failure in ceramic matrix minicomposites: experimental study and model, Acta Mater. 45 (1997) 1025–1044, https://doi.org/10.1016/S1359-6454(96)00224-8.
[12] J.W. Hutchinson, H.M. Jensen, Models of Fiber Debonding and Pullout in Brittle Composites with Friction, Elsevier, 1990, https://doi.org/10.1016/0167-6636(90)90037-G.
[13] G.N. Morscher, Modeling the elastic modulus of 2D woven CVI SiC composites, Compos. Sci. Technol. 66 (2006) 2804–2814, https://doi.org/10.1016/j.compscitech.2006.02.030.
[14] N.P. Bansal, J. Lamon, Ceramic Matrix Composites: Materials, Modeling and Technology, John Wiley & Sons, 2014.
[15] E.B. Callaway, F.W. Zok, Tensile response of unidirectional ceramic minicomposites, J. Mech. Phys. Solids 138 (2020), https://doi.org/10.1016/j.jmps.2020.103903.
[16] G.N. Morscher, J.D. Cawley, Intermediate temperature strength degradation in SiC/SiC composites, J. Eur. Ceram. Soc. 22 (2002) 2777–2787, https://doi.org/10.1016/S0955-2219(02)00144-9.
[17] W.A. Curtin, Fiber pull-out and strain localization in ceramic matrix composites, J. Mech. Phys. Solids 41 (1993) 35–53, https://doi.org/10.1016/0022-5096(93)90062-K.
[18] R.S. Goldberg, A.S. Almansour, R.M. Sullivan, Analytical Simulation of Effects of Local Mechanisms on Tensile Response of Ceramic Matrix Minicomposites, NASA/TM-20210012652.
[19] J. Lamon, F. Rebillat, A.G. Evans, Microcomposite test procedure for evaluating the interface properties of ceramic matrix composites, J. Am. Ceram. Soc. 78 (1995) 401–405, https://doi.org/10.1111/j.1151-2916.1995.tb08814.x.
[20] A. Chulya, J.P. Gyekenyesi, R.T. Bhatt, Mechanical behavior of fiber reinforced SiC/RBSN ceramic matrix composites: theory and experiment, 36th Int. Gas Turbine Aeroengine Congr. Expo. (1991).
[21] S. Mazerat, R. Pailler, Dataset on fractographic analysis of various SiC-based fibers, Data Br. 34 (n.d.) 106676. doi: https://doi.org/10.1016/j.dib.2020.106676.
[22] E.B. Callaway, F.W. Zok, Strengths of ceramic fiber bundles: theory and practice, J. Am. Ceram. Soc. 100 (2017) 5306–5317, https://doi.org/10.1111/jace.15062.
[23] W.A. Curtin, Exact theory of fibre fragmentation in a single-filament composite, J. Mater. Sci. 26 (1991) 5239–5253, https://doi.org/10.1007/BF01143218.
[24] J. Lamon, B. Thommeret, C. Percevault, Probabilistic-statistical approach to matrix damage and stress–strain behavior of 2-D woven SiC/SiC ceramic matrix composites, J. Eur. Ceram. Soc. 18 (1998) 1797–1808, https://doi.org/10.1016/S0955-2219(98)00119-8.
[25] J.M. Neumeister, A constitutive law for continuous fiber reinforced brittle matrix composites with fiber fragmentation and stress recovery, J. Mech. Phys. Solids 41 (1993) 1383–1404, https://doi.org/10.1016/0022-5096(93)90085-T.
[26] C. Chateau, L. Gélébart, M. Bornert, J. Crépin, E. Boller, C. Sauder, W. Ludwig, In situ X-Ray microtomography characterization of damage in SiC$_f$/SiC minicomposites, Compos. Sci. Technol. 71 (2011) 916–924, https://doi.org/10.1016/J.COMPSCITECH.2011.02.008.
[27] C. Chateau, L. Gélébart, M. Bornert, J. Crépin, D. Caldemaison, C. Sauder, Modeling of damage in unidirectional ceramic matrix composites and multi-scale experimental validation on third generation SiC/SiC minicomposites, J. Mech. Phys. Solids 63 (2014) 298–319, https://doi.org/10.1016/j.jmps.2013.09.001.
[28] H. Serizawa, C.A. Lewinsohn, G.E. Youngblood, R.H. Jones, D.E. Johnston, A. Kohyama, Evaluation of Advanced SiC Fibers for Reinforcement of CMC, 1999, pp. 1–10.
[29] S. Mazerat, R. Pailler, Statistical data for the tensile properties and static fatigue of sic-based bundles, Data Br. 32 (2020) 106166, https://doi.org/10.1016/j.dib.2020.106166.
[30] E. Maillet, C. Baker, G.N. Morscher, V.V. Pujar, J.R. Lemanski, Feasibility and limitations of damage identification in composite materials using acoustic emission, Compos. Part A Appl. Sci. Manuf. 75 (2015) 77–83, https://doi.org/10.1016/j.compositesa.2015.05.003.
[31] E. Maillet, N. Godin, M. R'Mili, P. Reynaud, G. Fantozzi, J. Lamon, M. R'Mili, P. Reynaud, G. Fantozzi, J. Lamon, Real-time evaluation of energy attenuation: a novel approach to acoustic emission analysis for damage monitoring of ceramic matrix composites, J. Eur. Ceram. Soc. 34 (2014) 1673–1679, https://doi.org/10.1016/j.jeurceramsoc.2013.12.041.
[32] E. Maillet, N. Godin, M. R'Mili, P. Reynaud, G. Fantozzi, J. Lamon, Damage monitoring and identification in SiC/SiC minicomposites using combined acousto-ultrasonics and acoustic emission, Compos. Part A Appl. Sci. Manuf. 57 (2014) 8–15, https://doi.org/10.1016/j.compositesa.2013.10.010.
[33] N. Guel, Z. Hamam, N. Godin, P. Reynaud, O. Caty, F. Bouillon, A. Paillassa, Data merging of ae sensors with different frequency resolution for the detection and identification of damage in oxide-based ceramic matrix composites, Materials (Basel) 13 (2020) 1–22, https://doi.org/10.3390/ma13204691.